



ISTITUTO NAZIONALE DI RICERCA METROLOGICA Repository Istituzionale

Size-dependent catalytic effect of magnetite nanoparticles in the synthesis of tunable magnetic polyaniline nanocomposites

This is the author's accepted version of the contribution published as:

Original

Size-dependent catalytic effect of magnetite nanoparticles in the synthesis of tunable magnetic polyaniline nanocomposites / Falletta, Ermelinda; Ferretti, Anna M.; Mondini, Sara; Evangelisti, Claudio; Capetti, Elena; Olivetti, Elena Sonia; Martino, Luca; Beatrice, Cinzia; Soares, Gabriel; Pasquale, Massimo; Della Pina, Cristina; Ponti, Alessandro. - In: CHEMICKÉ ZVESTI. - ISSN 0366-6352. - 75:10(2021), pp. 5057-5069. [10.1007/s11696-021-01604-z]

Availability:

This version is available at: 11696/73570 since: 2022-02-23T17:57:04Z

Publisher:

SPRINGER INTERNATIONAL PUBLISHING AG

Published

DOI:10.1007/s11696-021-01604-z

Terms of use:

This article is made available under terms and conditions as specified in the corresponding bibliographic description in the repository

Publisher copyright
SPRINGER NATURE

This version of the article has been accepted for publication, after peer review (when applicable) and is subject to Springer Nature's AM terms of use, but is not the Version of Record and does not reflect post-acceptance improvements, or any corrections.

(Article begins on next page)

1 **Size-dependent catalytic effect of magnetite nanoparticles in the synthesis of**
2 **tunable magnetic polyaniline nanocomposites**

3
4 **Ermelinda Falletta^{1*}, Anna M. Ferretti², Sara Mondini², Claudio Evangelisti^{2†}, Elena**
5 **Capetti², Elena Sonia Olivetti³, Luca Martino³, Cinzia Beatrice³, Gabriel Soares³,**
6 **Massimo Pasquale³, Cristina Della Pina¹, Alessandro Ponti^{2*}**

7 ¹*Department of Chemistry, University of Milan, via C. Golgi, 19, 20133, Milan (Italy)*

8 ²*Istituto di Scienze e Tecnologie Chimiche “Giulio Natta” (SCITEC), Consiglio Nazionale*
9 *delle Ricerche, via G. Fantoli 16/15, 20138, Milan (Italy)*

10 ³*Istituto Nazionale di Ricerca Metrologica (INRIM), Strada delle Cacce 91, 10135, Torino*
11 *(Italy)*

12
13 * Corresponding author, e-mail: alessandro.ponti@scitec.cnr.it, ermelinda.falletta@unimi.it

14
15 † Present address: Istituto di Chimica dei Composti Organometallici (ICCOM), Consiglio
16 Nazionale delle Ricerche, Via G. Moruzzi 1, 56124, Pisa (Italy)

17
18 **Abstract**

19 Nanocomposites comprising magnetic nanoparticles (NPs) embedded in an organic conducting
20 polymer are promising materials that may allow one to exploit synergic effects between the
21 electrically conducting and the magnetically permeable components. Having already shown
22 that magnetite NPs can be conveniently used as a catalyst for the oxidative polymerization of
23 the aniline dimer resulting in NPs embedded in the final composite and how to modulate the
24 magnetic coercivity of the composites, we now turn to investigate how the size of magnetite
25 NPs affects the polymerization and the properties of the final composite. Magnetite NPs of
26 diameter 2.3, 10, and 27 nm turned out to be effective catalysts with cheap oxidants such as
27 H₂O₂ and O₂. Yield data show that the rate-determining step occurs on the NP surface.
28 Extensive characterization shows that the NPs are well-dispersed in the composite with no
29 significant morphological change. The static magnetic properties of the composites are widely
30 different, e. g, the magnetic blocking temperature shifts from 290 K for 27 nm NPs to 54 K for
31 10 nm NPs while composites with 2.3 nm NPs are virtually unblocked down to 5 K. The
32 dynamic electromagnetic behavior studied up to the microwave range only shows energy
33 absorptions associated to the ferromagnetic resonance, at frequencies around 1 GHz.

34

35 **Keywords:** Fe₃O₄, PANI, magnetic nanoparticles, catalysis, electromagnetic absorption.

36

37

38

Introduction

39 Since their discovery, intrinsically conducting polymers (CPs) have emerged as outstanding
40 materials for numerous applications in many sectors, ranging from sensors (Wang *et al.*, 2020)
41 to biomedicine (Kaur *et al.*, 2015) passing from organic solar cells (Dong *et al.*, 2012),
42 environmental remediation (Ibanez *et al.*, 2018) and so on (Yang *et al.*, 2019; Li *et al.*, 2020).

43 Among CPs, polyaniline (PANI) is unique for its ease of synthesis, low cost, biocompatibility,
44 environmental stability, and extraordinary tunable properties (Badra *et al.*, 2009).

45 In recent years, materials combining characteristics and properties of two or more components
46 have been sought and required in many sectors. Among them, PANI/Fe₃O₄ nanocomposites
47 have been recently investigated as advanced materials being both electrically conducting and
48 magnetically permeable and having potential application in fields such as batteries (Wang *et al.*,
49 2017), electromagnetic interference shielding (Movassagh-Alanagh *et al.*, 2017),
50 environmental remediation (Muhammad *et al.*, 2019), cancer therapy (Ahmadkhani *et al.*,
51 2019),.

52 Several approaches have been developed to prepare these composites: mixing of PANI with
53 Fe₃O₄, self-assembly method, *in situ* polymerization, ultrasonic irradiation (Qiu *et al.*, 2006).

54 The ability of magnetite (and cobalt ferrite) nanoparticles (NPs) to act as catalysts in the PANI
55 synthesis was explored for the first time by us in the catalytic polymerization of *N*-4-
56 (aminophenyl)aniline (Della Pina *et al.*, 2012; Della Pina *et al.*, 2014; Della Pina *et al.*, 2015;
57 Falletta *et al.*, 2015). Most recently, Mišurović and coworkers applied Fe₃O₄ NPs as the catalyst
58 in the aniline polymerization (Mišurović *et al.*, 2019).

59 Exploiting magnetite NPs of different size to catalyze the polymerization of AD and prepare
60 PANI/Fe₃O₄ nanocomposites would allow one to tune the magnetic properties of the
61 composites provided that the NPs are size monodisperse and effective as a catalyst. The first
62 requirement can be met thanks to the well-established methods of size-controlled colloidal
63 nanochemistry (Ferretti *et al.*, 2021). As to the second one, the activity of a heterogeneous
64 catalysts is strongly related to its particle size since it is intrinsically dependent on the surface-
65 to-volume ratio, which dramatically grows passing from bulk to nano-dimensions. Moreover,
66 compared to bulk materials, NPs have a larger surface density of atoms in sites, such as corner
67 or edge sites, that maximize their reactivity because NPs are synthesized under kinetic control

68 and have spherical shape without the well-defined facets or crystals grown near thermodynamic
69 equilibrium. However, because of the small dimensions, the outstanding activity of
70 nanostructured materials is sometimes compromised by their strong interaction with
71 intermediates and by aggregation phenomena. To the best of our knowledge, the size-dependent
72 catalytic activity of Fe₃O₄ NPs in the oxidative polymerization of *N*-4-(aminophenyl)aniline
73 has not yet been investigated. Here, we report our recent results in the production and
74 characterization of conducting and magnetic PANI/Fe₃O₄ composites exploring at the same
75 time the effect of the Fe₃O₄ NP size on their catalytic activity and the variation of the
76 electromagnetic properties of the materials as function of the NP size.

77

78

79

Experimental

80 *Materials*

81 *Chemicals*

82 All chemicals were bought from Merck and used without any purification process. Acetone
83 (Aldrich) was distilled over KMnO₄ and stored under argon before use in the synthesis of 2.3
84 nm NPs.

85

86 *Synthesis of 2.3 nm magnetite NPs coated with oleic acid and derived from iron solvated metal* 87 *ions (SMA).*

88 The synthesis of Fe-SMA was carried out in a static metal vapor synthesis reactor described
89 elsewhere (Evangelisti *et al.*, 2015) and equipped with an alumina-coated tungsten crucible
90 heated by Joule effect with a generator with a maximum power of 2 kW. Fe-solvated metal
91 atoms (SMA) were prepared according to a previously described procedure (Barbaro *et al.*,
92 2015; Campisi *et al.*, 2019). Briefly, Fe vapors generated in high vacuum ($1 \cdot 10^{-5}$ mbar) by
93 resistive heating of an alumina-coated tungsten crucible, filled with approximately 300 mg of
94 iron, were co-condensed at -196 °C with acetone vapor (100 mL) in the glass reactor chamber
95 for 1 h. The reactor chamber was then warmed to the melting point of the solid matrix (ca. -95
96 °C), and the resulting brown Fe-solvated metal atoms (SMA) solution (95 mL) was siphoned
97 at a low temperature into a Schlenk tube under argon atmosphere. Oleic acid (1 mL) was added
98 to the Fe-SMA at low temperature (-40 °C) under gentle stirring, and then was left overnight at
99 room temperature to the open air. In these conditions, a red-brown precipitate was formed,
100 which was collected by centrifugation. The precipitate was dissolved in *n*-hexane (50 mL),
101 precipitated with acetone (50 mL) and collected by centrifugation. This latter procedure was

102 repeated three times to remove the excess of oleic acid. The solid was then dispersed in toluene
103 (75 mL). The iron content of the toluene dispersion, measured by the ICP-OES procedure
104 described below, resulted 2.60 g/L.

105

106 *Synthesis of 10.9 nm magnetite NPs coated with oleic acid.*

107 The NPs were synthesized by a modification of a published procedure (Hyeon *et al.*, 2001).
108 Oleic acid (2.68 mL, 8.51 mmol) was dissolved in dioctyl ether (12 mL) in a 100 mL three-
109 neck round-bottom flask, equipped with condenser and thermometer, under magnetic stirring
110 and N₂ atmosphere. The solution was subjected to three vacuum–N₂ cycles at RT and then
111 heated to 105 °C. Three vacuum–N₂ cycles were carried out at 105 °C. Next, iron pentacarbonyl
112 (280 µL, 2.13 mmol) was injected into the solution and the reaction mixture was heated to reflux
113 (*ca.* 285 °C) at a rate of 3 °C/min using a programmable heating unit. The solution turned black
114 after 50 min at reflux and was aged for an additional hour before cooling to RT. The NPs were
115 precipitated from the reaction mixture by adding acetone (60 mL), separated by centrifugation,
116 and dispersed in petroleum ether (45 mL). To further purify the NPs, acetone (60 mL) was
117 added to the NP dispersion and the NPs were collected by centrifugation and dispersed in
118 toluene (23 mL). The iron content of the toluene dispersion, measured by the UV-Vis procedure
119 described below, was 9.7 g/L.

120

121 *Synthesis of 26.0 nm magnetite NPs coated with oleic acid.*

122 The NPs were synthesized by a modification of a published procedure (Park *et al.*, 2004). The
123 metal precursor Fe(III) trioleate (FeOl₃) was synthesized as follows. Potassium oleate (5.77 g.,
124 18 mmol) and FeCl₃·6H₂O were dissolved in a mixture of H₂O (10 mL) and EtOH (12 mL) in
125 a 100 mL round-bottom flask under magnetic stirring and N₂ atmosphere. Hexane (21 mL) was
126 added to the reaction mixture, which was then heated to 70 °C for 4 h. After cooling to RT, the
127 mixture was transferred to a 100 mL separatory funnel and the aqueous phase discarded. The
128 red-brown organic phase was washed with deionized water (2 x 10 mL) and with saturated
129 aqueous NaCl solution (2 x 40 mL). The organic phase was evaporated under reduced pressure
130 and the waxy red-brown FeOl₃ dried under vacuum (rotary pump) at 50 °C (oil bath) for a few
131 hours. To synthesize the NPs, FeOl₃ (1.27 g, 1.52 mmol) and oleic acid (240 µL, 0.76 mmol)
132 were dissolved in trioctylamine (13 mL) in a 50-mL three-neck round-bottom flask, equipped
133 with condenser and thermometer, under magnetic stirring and N₂ atmosphere. The reaction
134 mixture was heated to reflux (*ca.* 360 °C) at a rate of 10 °C/3 min and aged for 30 min using a
135 programmable heating unit. After cooling to RT, the NPs were precipitated from the reaction

136 mixture by adding acetone (60 mL), separated by centrifugation, and dispersed in toluene (15
137 mL). To purify the NPs, this procedure was repeated two more times. The iron content of the
138 toluene dispersion, measured by the UV-Vis procedure described below, was 0.68 g/L. Such
139 low concentration was required to ensure colloidal stability of these NPs.

140

141 *Determination of the iron content of NP dispersions*

142 ICP-OES procedure. The Fe content in SMA-derived NPs was determined by inductively
143 coupled plasma-optical emission spectroscopy (ICP-OES) (ICAP 6300 Duo, Thermo Fisher
144 Scientific) and an external calibration methodology. The limit of detection (LOD) calculated
145 for iron as 5 ppb. For the analysis, the toluene dispersion of SMA-derived NPs (0.5 mL) was
146 heated in a porcelain crucible over a heating plate and the solvent was evaporated. The solid
147 residue was dissolved in aqua regia (2 mL), heated until complete evaporation and the solid
148 residue was then dissolved in 0.5 M aqueous HCl. The iron content was then measured by ICP-
149 OES.

150 UV-Vis procedure. This procedure is described in detail in (Mondini *et al.*, 2015) and is here
151 briefly outlined. About 0.1 mL of toluene NP dispersion is dissolved in aqua regia and
152 evaporated. The residue is re-dissolved in 0.1 M HCl and the solution is buffered with PBS (pH
153 7). The solution is then treated with tiron in excess to form the red iron complex $[\text{Fe}(\text{tiron})_3]^{3-}$
154 that is spectrophotometrically determined by a calibration method.

155

156 *PANI/Fe₃O₄NPs composites preparation using H₂O₂ as the oxidant*

157 500 mg of *N*-4-(aminophenyl)aniline (aniline dimer, AD) were dispersed in 30 mL of water
158 acidified with 2.7 mL of HCl 1 M (AD/HCl = 1, molar ratio). The mixture was stirred for 30
159 minutes. Then, 1.2 mL of an aqueous of H₂O₂ 35% was added (H₂O₂/AD = 5, molar ratio,
160 followed by different amounts of Fe₃O₄ NPs. After 24 h, a dark green solid was recovered by
161 filtration, washed with water and acetone abundantly until clearness of the mother liquors and
162 dried in an oven at 60°C until it reached a constant weight.

163

164 *PANI/Fe₃O₄NPs composites preparation using O₂ as the oxidant*

165 500 mg of *N*-4-(aminophenyl)aniline (aniline dimer, AD) were dispersed in 30 mL of water
166 acidified with 2.7 mL of HCl 1 M (AD/HCl = 1, molar ratio). The mixture was stirred for 30
167 minutes and then different amounts of Fe₃O₄ NPs were added. The reaction mixture was stirred
168 under pressure of molecular oxygen (3 bar) for 72 h at 80°C. Finally, a dark green solid was

169 recovered by filtration, washed with water and acetone abundantly until clearness of the mother
170 liquors and dried in an oven at 60°C until it reached a constant weight.

171

172 *Materials Characterization*

173 The TEM images, electron diffraction (ED) patterns, Electron Energy Loss Spectroscopy
174 (EELS) data, and Energy Filtered (EF-TEM) TEM images were recorded by a ZEISS LIBRA
175 200FE TEM that operates at 200kV and is equipped with a second generation in-column Ω
176 filter and a HAADF detector for STEM imaging. The samples were prepared by dropping 7 μ l
177 of NP dispersion on a copper grid coated with a 1-3 nm carbon film and letting it dry overnight.
178 The magnetite NPs were colloiddally dispersed in toluene, whereas the composite samples were
179 suspended in isopropanol. TEM and EF-TEM Images were processed by means of the iTEM
180 TEM Imaging Platform software (Olympus) and the NP size distribution was measured by the
181 software PEBBLES (Mondini, *et al.*, 2012).

182 FT-IR spectra of composites were recorded in the transmittance mode in the range 500-4000
183 cm^{-1} at 64 scans per spectrum and a 2 cm^{-1} resolution by JASCO FT/IR-410 spectrophotometer
184 (JASCO Corporation, Tokyo, Japan). A small amount of each sample was dispersed in KBr and
185 compressed in 13 mm diameter pellets with a 10-ton hydrostatic press for 15 min.

186 X-ray powder diffraction (XRPD) analyses were carried out in a 2θ range between 10° and
187 80° on a Philips PW 3710 Bragg-Brentano goniometer (Philips, Amsterdam, Netherlands)
188 equipped with a scintillation counter, a slit with 1° divergence, a receiving slit of 0.2 mm and a
189 0.04° Soller slit system. A graphite-monochromatic Cu $K\alpha$ radiation was adopted at a nominal
190 X-ray power of 40 kV \times 40 mA.

191 The metal loss in the Fe₃O₄/PANI composites was determined by atomic absorption
192 spectroscopy on a AAAnalyst 100 PerkinElmer instrument.

193 Magnetization measurements of composites synthesized using H₂O₂ were carried out by a
194 Quantum Design MPMS XL-5 SQUID magnetometer. Weighted amounts of composite were
195 sealed in Teflon tape. Field-cooled (FC) and zero-field-cooled (ZFC) magnetization curves
196 were recorded in the 5-300 K range. After cooling the sample from 300 to 5 K in zero field, the
197 ZFC magnetization was recorded on heating to 300 K using a measuring field $H_{\text{meas}} = 10$ Oe.
198 Next, the FC magnetization was measured ($H_{\text{meas}} = 10$ Oe) while cooling the sample from 300
199 to 5 K under $H_{\text{cool}} = 10$ Oe. In the case of the sample with the largest NPs (PANI/NP27), the
200 highest temperature was set to 350 K. Magnetization isotherms (hysteresis loops) were recorded
201 between +50 kOe and -50 kOe at 5 K after cooling in zero magnetic field. All data were
202 corrected for the diamagnetism of the sample holder and PANI and then scaled to the NP mass.

203 The ac magnetic properties were determined using an Agilent 4395A impedance analyzer using
204 a coaxial short 16454A magnetic material test fixture, and a test of the dielectric properties was
205 performed using a parallel plate method with the 16453A dielectric material test fixture.

206

207

208

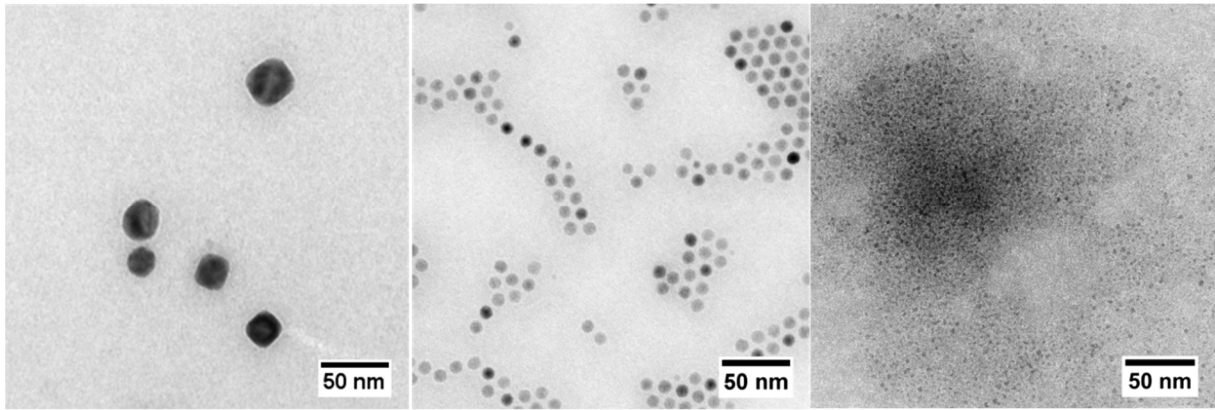
Results and discussion

209 *Magnetite nanoparticles*

210 To study how the NP size affects the catalytic polymerization of AD and the properties of the
211 resulting nanocomposite, we prepared magnetite NPs of different size by different procedures,
212 each yielding NPs with good size dispersity and uniform shape. We used thermal decomposition
213 to prepare medium and large NPs (Hyeon *et al.*, 2001; Park *et al.*, 2004), whereas very small
214 NPs were synthesized by metal vapor synthesis technique (Barbaro *et al.*, 2015; Campisi *et al.*,
215 2019). TEM images of the NP samples are reported in Figure 1. We obtained the NP
216 morphological parameters by analyzing the TEM images using the Pebbles software
217 (Mondini, *et al.*, 2012) and collected them in Table 1 (The histograms of the NP diameter can
218 be found in the ESI) The three NP samples have largely different size: the diameters span more
219 than an order of magnitude (2.3 to 27 nm) while the surface (related to the catalytic activity)
220 and the volume (related to the magnetic properties of the composite) span more than two and
221 three orders of magnitude, respectively. The size dispersion is good to excellent. The 28%
222 dispersion of NP2 may seem large but one should note that the standard deviation of 0.64 nm
223 is smaller than the magnetite cell size (0.84 nm). All NPs have spherical shape, except for the
224 largest nanoparticles in NP27 that display cuboidal shape (see ESI for further TEM images of
225 NP27). The crystal phase of the NP27 and NP10 samples was confirmed to be spinel (cubic
226 ferrite) by ED (see ESI). No diffraction ring can be seen in the ED pattern of NP2 NPs. As
227 already reported (Barbaro *et al.*, 2015), such small NPs are crystalline, and the absence of
228 diffraction rings can then be ascribed to the very wide breadth of the rings. Finally, we note that
229 in this paper, for the sake of clarity, we use the term “magnetite” or “Fe₃O₄” NPs to indicate
230 iron oxide NPs with cubic ferrite crystal structure and composition Fe_{3-x}O_{4-x} ($0 \leq x \leq 1$), varying
231 between magnetite and maghemite.

232

233



234

235 **Figure 1.** TEM images of as synthesized NPs. a) NP27, b) NP10 c) NP2.

236

237 **Table 1.** Parameters of the distribution of the diameter of as-synthesized magnetite NPs. The
 238 number of measured NPs N is reported along with the mean, standard deviation, and variation
 239 coefficient of the diameter distribution.

Sample	N	Mean (nm)	Standard deviation (nm)	Variation coefficient (%)
NP2	463	2.3	0.64	28
NP10	1417	10.0	0.43	4.3
NP27	181	27.1	4.3	16

240

241

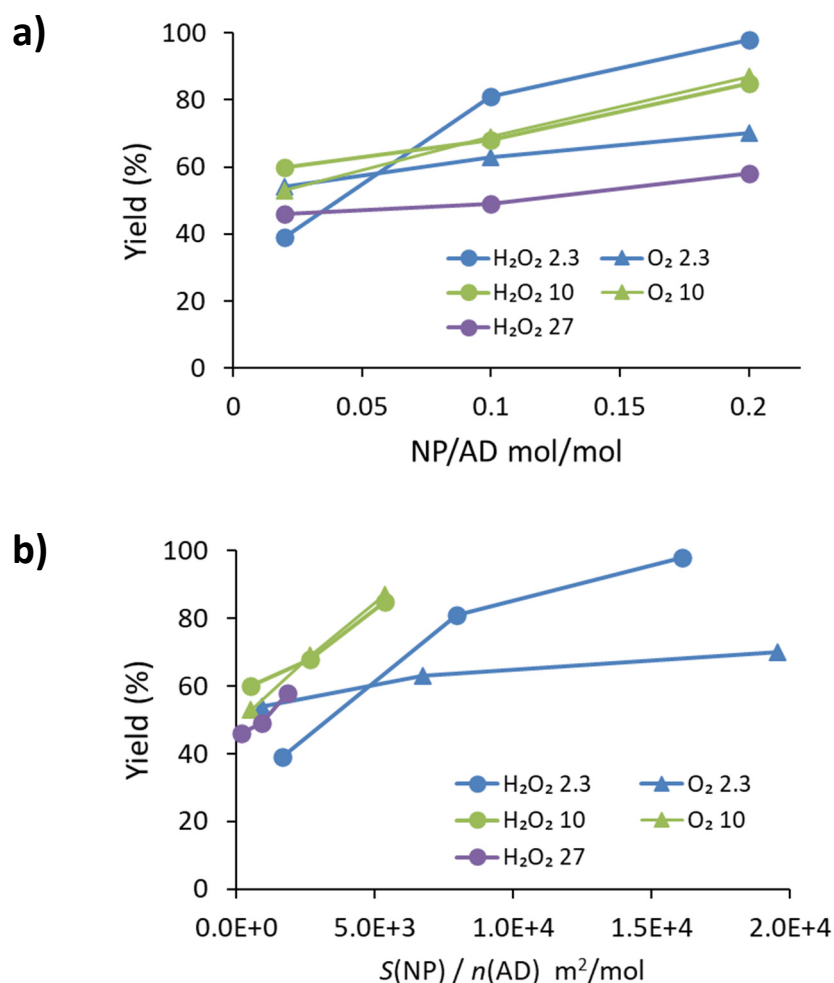
242 *Polymerization of AD in the presence of Fe_3O_4 nanoparticles*

243 The dependence of the catalytic activity of Fe_3O_4 NPs on their size was evaluated in the AD
 244 oxidative polymerization. The catalytic performance of the NPs is assessed keeping in mind
 245 that the NPs are both the catalyst and the magnetic load.

246 In Figure 2 the yield (mass %) of composites PANI/ Fe_3O_4 NPs is plotted versus the NP/AD
 247 molar ratio, where the numerator is the amount of Fe_3O_4 contained in the NPs.

248

249



250 **Figure 2.** Yield (mass %) of composite from the AD polymerization in the presence of
 251 magnetite NPs. The yield is plotted as a function of (a) the NP/AD molar ratio and (b) the ratio
 252 of the NP surface area S to the molar amount n of AD.

253

254 The NP/AD molar ratio was chosen so to explore a NP/AD range that would reasonably yield
 255 composites with the desired electrical and magnetic properties. As previously reported, the
 256 oxidant used for the polymerization reaction (H₂O₂ or O₂) does not significantly affect the
 257 properties of the PANI/Fe₃O₄ composites (Della Pina *et al.*, 2012). Because H₂O₂ is especially
 258 attractive for the liquid-phase oxidation, due to the high percentage of active oxygen and the
 259 production of water as only by-product, we here focused on composites obtained using H₂O₂.
 260 Polymerizations carried out using O₂ as the oxidant are included for comparison.

261 In all experimental conditions explored, the yield increases with the amount of NPs, confirming
 262 the catalytic role of the NPs. More insight can be gained when the yield is plotted as a function
 263 of the ratio $S/n(AD)$, where S is the total core surface area of the NPs and $n(AD)$ is the molar
 264 amount of AD (Figure 2b). The area S is estimated from the total mass of Fe₃O₄ in the composite

265 m and their mean surface area $\langle s \rangle$ and volume $\langle v \rangle$ measured from TEM images as $S = m \langle s \rangle$
266 / $\rho \langle v \rangle$, where $\rho = 5.17 \text{ g/cm}^3$ is the density of magnetite. When small NP2 are used, a
267 significant fraction of the NPs is not embedded in the final composite (see ESI). We corrected
268 the data for NP2 in Figure 2b by considering the surface of embedded NPs only. The lack of
269 smallest NPs can be attributed to their very high surface area that makes them more sensitive
270 to the environment. The stability of such small particles is difficult to study and aggregation
271 and dissolution phenomena have to be considered.

272 The yield vs. $S/n(\text{AD})$ data for the larger NPs (NP10 and NP27) is scarcely affected by the NP
273 size or oxidant. They cluster along a straight line, indicating that the slow initial steps of the
274 polymerization (Tzou and Gregory, 1992) occur on the surface of the NP inorganic core. This
275 linear behavior extends to high conversion, suggesting that the NPs are stable against
276 aggregation in the reaction conditions.

277 The yield of NP2 is always lower than that of the larger NPs. When H_2O_2 is used as an oxidant,
278 the yield data of NP2 is parallel to that of the larger NPs but shifted to the right (Figure 2b).
279 This suggests that partial NPs aggregation occurs during the polymerization, as confirmed by
280 TEM (see Figure 4 below), thus decreasing the available active sites for the AD oligomerization
281 and hindering transport of AD to them. When $\text{NP/AD} = 0.2 \text{ mol/mol}$, parallelism is lost as the
282 yield levels off because most of the AD has undergone polymerization. When NP2 are used
283 with O_2 , the yield at $\text{NP/AD} = 0.02 \text{ mol/mol}$ is comparable to that of the larger NPs showing
284 that the NP surface is as active as in the other cases. However, the yield increases very slowly
285 with the $S/n(\text{AD})$ ratio. We admit that we could not find a better explanation for this behavior
286 than invoking extensive NP aggregation when the NP/AD ratio is larger than 0.02 and O_2 is
287 used as an oxidant.

288 In summary, magnetite NPs with size from 2.3 to 27 nm are able to catalyze the polymerization
289 of AD, using either H_2O_2 or O_2 as oxidant, and with yield ranging from 39% to 98%. It is
290 therefore feasible to produce magnetic PANI composites with magnetite NPs spanning a size
291 range wider than an order of magnitude.

292

293 *PANI/Fe₃O₄NPs characterization*

294 All composites were characterized by different techniques in order to investigate the effect of
295 the presence of the magnetic NPs in the final materials. Here, we report the results obtained for
296 the composites synthesized in the presence of H_2O_2 as the oxidant and using a NP/AD molar
297 ratio of 0.2, because they are the most representative. These three composites are named
298 PANI/NP2, PANI/NP10, and PANI/NP27.

299 The amount of magnetic NPs inside the composites was indirectly evaluated by the analysis of
300 iron in the mother liquors obtained after the filtration of the materials. The results show that
301 only for the composite PANI/NP2 the content of NPs within the polymeric matrix is not
302 quantitative (16% of Fe₃O₄, cfr. ESI). In all other cases, during the polymerization reaction the
303 inorganic component is completely embedded in the polymeric matrix (33% of Fe₃O₄ in
304 PANI/NP10, 31% of Fe₃O₄ in PANI/NP27).

305

306 *Fourier-transform infrared (FT-IR) spectroscopy*

307 All composites comprise a polymeric matrix consisting of PANI in the form of conducting
308 emeraldine, as shown by characteristic infrared bands (see ESI). In particular, the broad band
309 between 3400-1800 cm⁻¹ confirms that the polymer was obtained in highly conjugated form
310 (Šeděnková *et al.*, 2008), the band at 1570 and 1490 cm⁻¹ are assigned to the C=C stretching
311 vibration of quinoid and benzenoid rings respectively, whereas C-N stretching vibration is
312 responsible of the band at 1304 cm⁻¹ (Cionti *et al.*, 2020). The band at 1240 cm⁻¹ is due to C-
313 N^{+•} stretching vibration (Šeděnková *et al.*, 2008) and that to 1146 cm⁻¹ derives from Q=NH⁺-
314 B, B-NH⁺-B stretching (Mišurović *et al.*, 2019). C-H out-of-plane bending vibrations of 1,4-
315 disubstituted aromatic rings lead to the bands in the 820-800 cm⁻¹ range (Socrates, 2004).
316 Finally, the two bands at 800 and 759 cm⁻¹ suggest the presence of C-H vibrations of 1,2,4-
317 trisubstituted and 1,2-disubstituted rings (Socrates, 2004).

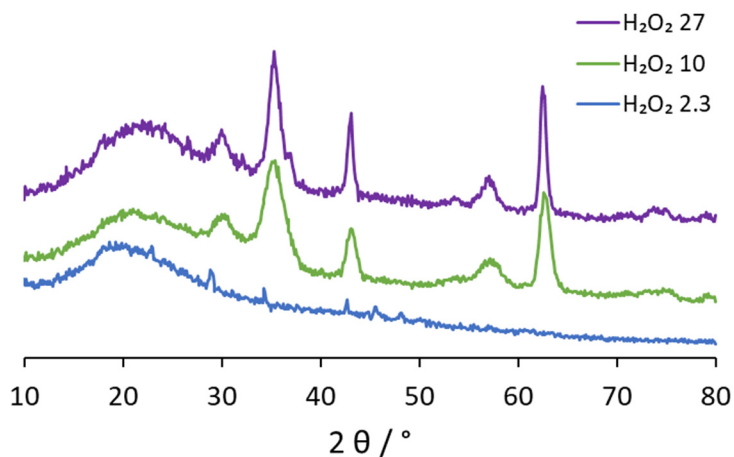
318

319 *X-ray powder diffraction (XRPD)*

320 The XRPD patterns of PANI/Fe₃O₄NPs composites are reported in Figure 3.

321

322



323

Figure 3. XRPD patterns of PANI/Fe₃O₄NPs composites.

324

325

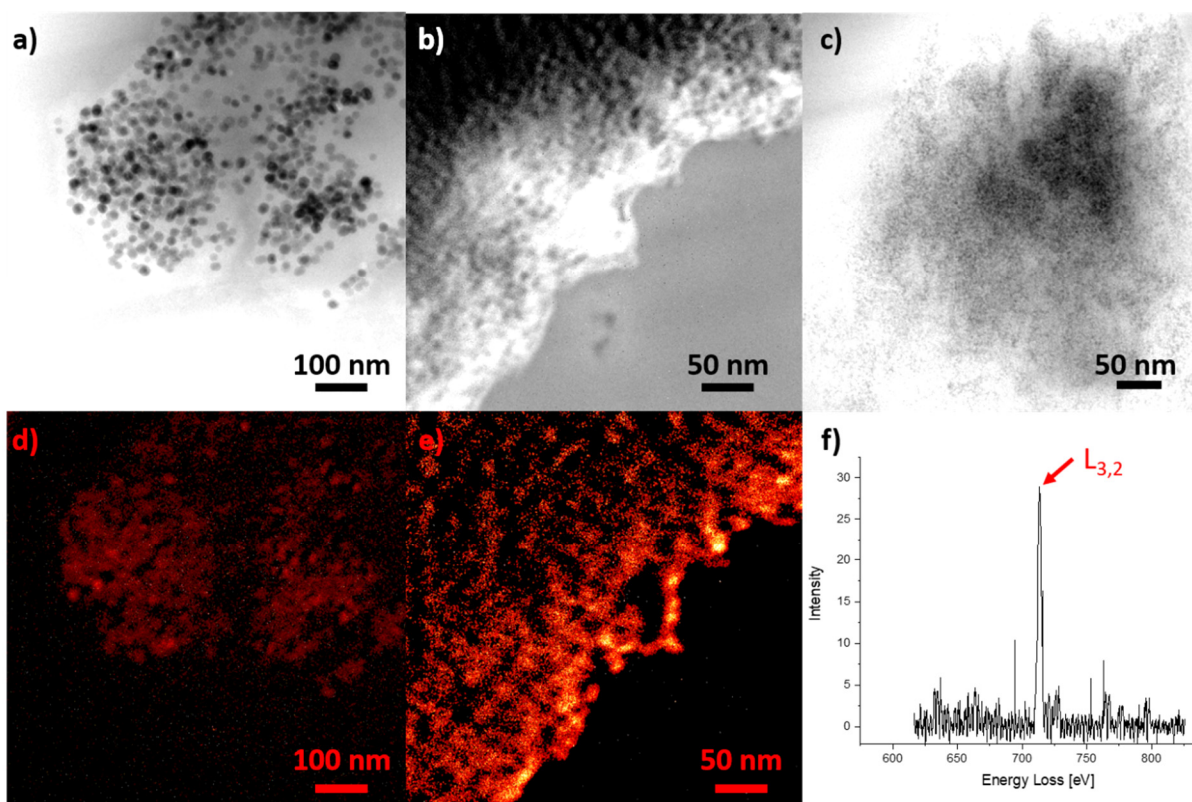
326 The XRPD patterns of the composites show the typical Bragg diffraction peak at $2\theta \approx 20^\circ$ for
327 the polymer. Peaks at $2\theta = 30.1, 35.6, 43.2, 53.8, 57.2,$ and 63.0° are prominent in the patterns
328 of composites including NP10 and NP27. They can be assigned to cubic ferrite (spinel) NPs,
329 showing that during the synthesis of the composites the magnetic NPs were embedded into the
330 polymer. The XRPD pattern of PANI/NP2 composites only shows the peak of PANI. Since the
331 presence of small NP2 in the composite is established by TEM techniques (see the net section),
332 the absence of the peaks typical of the spinel structure could be due to the amorphousness of
333 the NPs. However, NP2 were already shown to be crystalline (Barbaro *et al.*, 2015). Therefore,
334 the inability to detect the spinel peaks is ascribed to combined effect of the larger peak width
335 expected for smaller NPs (about fourfold wider than for PANI/NP10) and the lower magnetite
336 content in PANI/NP2.

337

338 *TEM microscopy*

339 The TEM investigation of the composites has two goals: to establish the presence of magnetite
340 NPs within the composites and to ascertain whether the NPs underwent morphological changes
341 during the polymerization reaction. The investigation could not rely on conventional TEM
342 imaging only because the composite granules are thick enough to be opaque to the electron
343 beam except for the very edges of the granules (see ESI).

344



345

346 **Figure 4.** TEM of PANI/Fe₃O₄NPs composites. EF-TEM images filtered at 30 eV of a)
 347 PANI/NP27, b) PANI/NP10, and c) PANI/NP2. False-color EF-TEM images filtered at 713 eV
 348 providing Fe maps of d) PANI/NP27 and e) PANI/NP10. The sample regions imaged are the
 349 same as in a) and b). f) Background-subtracted EELS spectrum of PANI/NP2 showing the iron
 350 $L_{3,2}$ peak.

351

352 We thus resorted to energy-filtered TEM (EF-TEM) techniques by which the image is formed
 353 by detecting electrons that lost energy during the interaction with sample (Figure 4). In images
 354 filtered at 30 eV loss, the contrast between NPs and polymer is enhanced since electrons can
 355 lose 30 eV only by interacting with nearly-free aromatic π electrons, the so-called plasmonic
 356 mode, so that the polymer matrix appears light gray whereas the NPs appear dark. The enhanced
 357 contrast between NPs and polyaniline allowed us to identify the NPs inside the composite
 358 (Figure 4a-c). The NPs are well dispersed within the composites. Some NP agglomeration was
 359 observed in the case of the PANI/NP2 (dark region in Figure 4c). NP measurement was
 360 unfortunately reliable only for PANI/NP10 and PANI/NP27. The results are collected in Table
 361 2. Comparing this data with those in Table 1, one can see that the NP10 are unchanged while
 362 the NP27 decreased in size by about 2 nm during the polymerization. In both cases, the size

363 dispersion is unchanged. We can therefore expect that the properties of the magnetic NPs are
 364 unaffected by the polymerization, except for what relates to the interparticle distance.

365

366 **Table 2.** Parameters of the distribution of the diameter of magnetite NPs present in
 367 PANI/Fe₃O₄NPs composites. The number of measured NPs N is reported along with the
 368 mean, standard deviation, and variation coefficient of the diameter distribution.

Composite	N	Mean (nm)	Standard deviation (nm)	Variation coefficient (%)
PANI/NP10	335	10.2	0.63	6.2%
PANI/NP27	207	25.0	4.6	18%

369

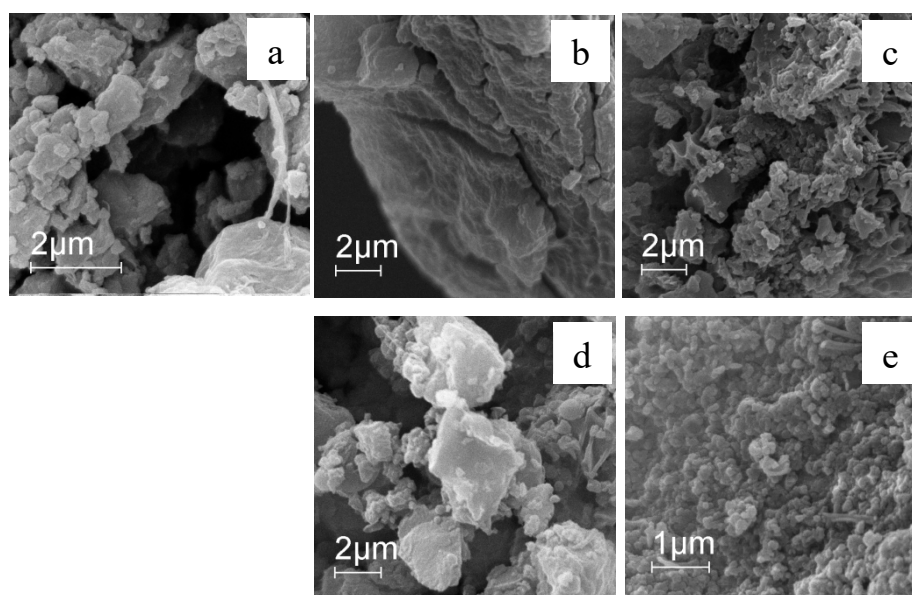
370

371 We also confirmed the presence of iron in the embedded NPs detecting electrons with energy
 372 loss of 713 eV, typical of iron ($L_{2,3}$ peak). The EF-TEM iron maps of PANI/NP27 and
 373 PANI/NP10 (Figure 4d,e) show that the iron signal coincides with the NPs as seen in the
 374 corresponding 30 eV loss images (Figure 4a,b). In the case of PANI/NP2, the intensity of the
 375 EF-TEM iron map was too low to reliably identify the NPs within the composite. The presence
 376 of iron in PANI/NP2 was established thanks to the EELS spectrum that displays the iron $L_{3,2}$,
 377 peak at 713 eV (Figure 4f). The crystal structure of the embedded NPs was analyzed by ED
 378 (see ESI): the ED patterns confirmed that PANI/NP27 and PANI/NP10 comprise cubic ferrite
 379 NPs. PANI/NP2 gave no detectable diffraction rings.

380

381 *SEM microscopy*

382 In Figure 5, SEM images of PANI/Fe₃O₄NPs composites are displayed.



383

384 **Figure 5.** SEM images of PANI/Fe₃O₄NPs composites (a: PANI/NP27, b: PANI/NP10, c:
385 PANI/NP2) or O₂ as oxidant (d: PANI/NP10, e: PANI/NP2).

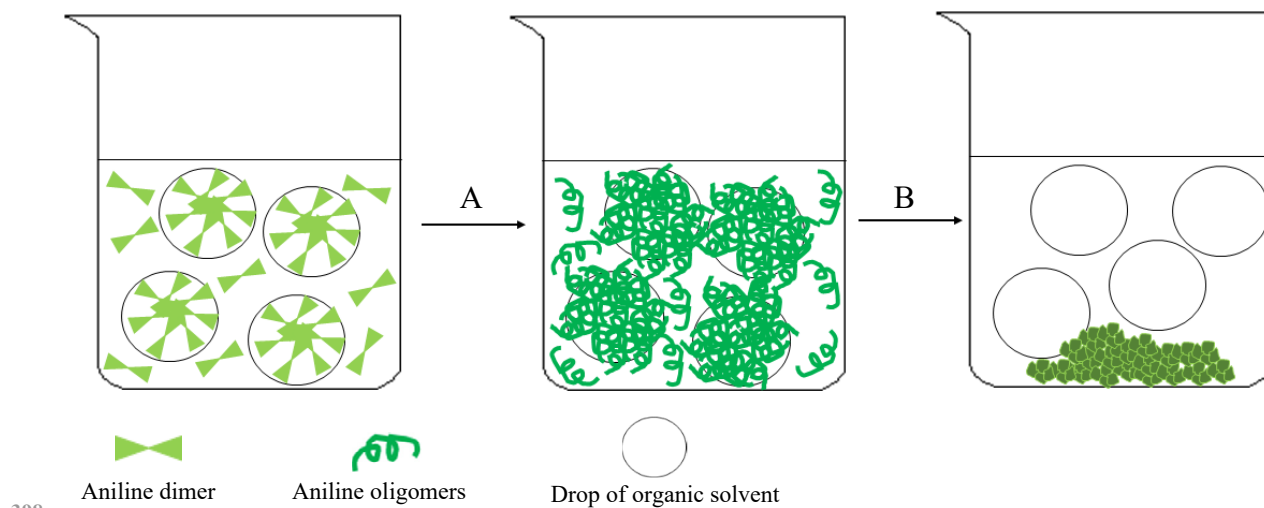
386

387 When compared to PANI obtained by the oxidative polymerization of AD in the presence of a
388 homogeneous catalyst, e.g., Fe(III) (Della Pina *et al.*, 2018), PANI/Fe₃O₄NPs composites
389 display a more globular morphology, sparsely intermixed with nanorods. As previously
390 reported (Della Pina *et al.*, 2012), when AD hydrochloride is polymerized by H₂O₂ in water in
391 the presence of magnetite NPs dispersed in an organic phase as the catalyst, an interfacial
392 polymerization occurs. Thanks to its solubility in organic solvents, AD hydrochloride can
393 diffuse into the organic phase where Fe₃O₄ NPs are present, and the oxidative polymerization
394 can take place at the interface between the organic and aqueous phases (Scheme 1).

395

396

397



399 **Scheme 1.** Proposed mechanism of nanoglobules formation. A) oligomerization step, B)
400 polymerization step.

401

402 During the first steps of the reaction, only PANI oligomers are produced that are soluble in
403 organic solvents and, as a consequence, they can diffuse inside the toluene drops. When the
404 polymeric chains grow longer, they become insoluble and precipitate from the reaction mixture
405 leading to globular materials.

406 Even though this hypothesis of mechanism seems to be in contrast with that previously reported
407 (Della Pina *et al.*, 2012), it has to be considered that the amount of organic phase was changed
408 and the catalysts were obtained by a different synthetic approach (co-precipitation reaction in
409 Della Pina *et al.*, 2012, thermal decomposition here).

410

411 *Magnetic properties*

412 The thermal behavior of the magnetization M of the PANI/Fe₃O₄NPs composites (oxidant:
413 H₂O₂; NP/AD = 0.02 mol/mol) was investigated by means of ZFC/FC experiments (Figure 6).
414 The main magnetic parameters are collected in Table 3. The ZFC/FC curves of the composites
415 are widely different. Reversible behavior is indicated by the identity of the ZFC and FC data,
416 which is clearly visible in the high temperature range for all composites. The reversibility
417 corresponds to the superparamagnetic (SPM) regime where thermal agitation quickly flips the
418 NP magnetization. Upon cooling the two curves diverge as soon as thermal agitation is not able
419 to overcome the barrier for magnetization reversal of some NPs and irreversibility sets in. The
420 irreversibility temperature T_{irr} , defined as the temperature at which the difference between the
421 FC and the ZFC magnetization $(M_{FC} - M_{ZFC})/M_{FC} = 3\%$, is larger than RT for PANI/NP27, as
422 low as 110 K for PANI/NP10, and probably less than 80 K for PANI/NP2 (in the latter case,

423 the smallness of $M_{FC}-M_{ZFC}$ prevents an accurate determination of T_{irr}). Thus, PANI/NP27
 424 contains NPs both in the SPM and blocked regime even at RT, in agreement with the ideal RT
 425 blocking diameter of magnetite (26 nm) (Coey, 2010).

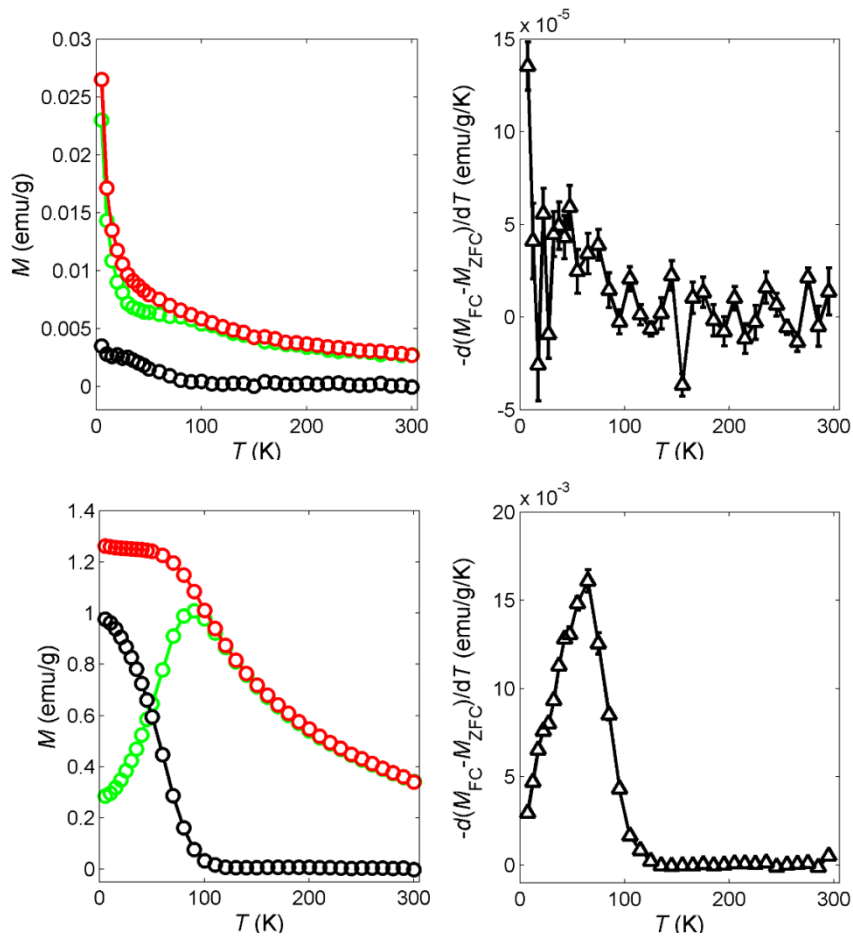
426

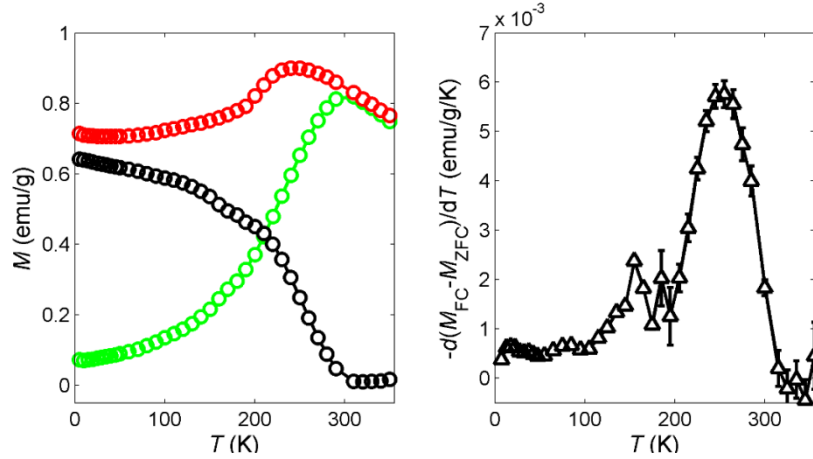
427 **Table 3.** Magnetic parameters of the ZFC/FC magnetization of PANI/Fe₃O₄NPs composites.

Composite	T_{irr} (K)	T_{der} (K)	HWHH	
			(K)	$\langle T_b \rangle$ (K)
PANI/NP2	< 80 K	–	–	–
PANI/NP10	110	60	29	54
PANI/NP27	310	250	41	290

428

429





430 **Figure 6.** Thermal behavior of the low-field ($H = 10$ Oe) magnetization of PANI/Fe₃O₄NPs
 431 composites. In the left panels, the ZFC (green) and FC (red) magnetizations are shown along
 432 with their difference (black). In the right panels, the $-d(M_{FC}-M_{ZFC})/dT$ derivative is plotted to
 433 represent the distribution of the blocking temperatures. Top: PANI/NP2, middle: PANI/NP10,
 434 bottom: PANI/NP27. The error bars represent 1 standard deviation; the error bars are not visible
 435 when the standard deviation is smaller than the symbol size.

436

437 Upon further cooling below T_{irr} , more NPs enter the blocked regime. In this temperature region,
 438 the three samples display largely different behavior. M_{FC} and M_{ZFC} of PANI/NP2 are similar
 439 down to 5 K, showing that the NPs in this composite are subject to low barriers for
 440 magnetization rotation, as expected for very small NPs. PANI/NP10 displays a strong decrease
 441 of M_{ZFC} and a flattening of M_{FC} at low temperature. The larger difference between M_{FC} and
 442 M_{ZFC} corresponds to larger barriers. The M_{FC} and M_{ZFC} of PANI/NP10 and PANI/NP2 are
 443 typical of weakly interacting NPs. In the case of PANI/NP27, both M_{FC} and M_{ZFC} decrease from
 444 250 K down to 5 K, showing strong interparticle interactions and the onset of a frozen spin-
 445 glass-like state where the magnetization is frozen in one of the many minima of a complex free-
 446 energy landscape created by the magnetostatic interaction among the NPs. The presence and
 447 freezing temperature of the spin-glass-like state agree with an estimate of the relative strength
 448 of the magnetostatic interaction among the NPs (see ESI).

449 A representation of the magnetization rotation barriers of a composite (in terms of blocking
 450 temperature T_b) can be obtained as the derivative of the difference between the FC and ZFC
 451 magnetization $-d(M_{FC}-M_{ZFC})/dT$ (Figure 6, right panels) (Bruvera *et al.*, 2015). This
 452 representation faithfully displays the distribution of T_b in the case of weakly-interacting NPs.
 453 When a spin-glass-like state sets in, the concept of T_b of individual NPs is not appropriate but
 454 $-d(M_{FC}-M_{ZFC})/dT$ however provides useful information about the barriers, (Woińska *et al.*,

455 2013) though they are a property of the whole sample and cannot be tied to individual NPs. The
 456 mode T_{der} and half-width-half-height (HWHH) of the T_b distribution can be found in Table 3
 457 along with the mean barrier $\langle T_b \rangle$. PANI/NP2 has barriers with $T_b < 80$ K but T_{der} and $\langle T_b \rangle$
 458 could not be reliably determined. These barriers, which are related to a small part of the total
 459 magnetization, as shown by the $M_{\text{FC}} - M_{\text{ZFC}}$ difference, can be attributed to a few NP aggregates.
 460 The barriers in PANI/NP10 are distributed about $T_{\text{der}} = 60$ K ($\langle T_b \rangle = 54$ K) and extend down
 461 from 100 K (HWHH 29 K). A similar peak is observed in the PANI/NP27 T_b distribution, but
 462 it occurs at higher $T_{\text{der}} = 250$ K ($\langle T_b \rangle = 290$ K) with HWHH = 41 K. The barrier distribution
 463 has a broad tail extending down to 5 K, which is related to collective barriers in the frozen state.
 464 The T_b of our composites agree with the T_b measured for magnetite NPs in the $d = 10$ -20 nm
 465 range (Yun *et al.*, 2014) (see ESI for a detailed comparison).

466 To gain more insight into the magnetic properties of the composites, magnetization isotherms
 467 were measured between -50 and $+50$ kOe at 5 K. The shape of these hysteresis loops (see ESI)
 468 and the magnetic parameters collected in Table 4 confirm the almost complete magnetic
 469 reversibility of PANI/NP2 at low temperature and the irreversible behavior of PANI/NP10 and
 470 PANI/NP27.

471 In summary, these composite materials display a variety of magnetic behavior that can be
 472 selected by choosing the NP size, e.g., the SPM regime can be shifted from RT to $T \approx 5$ K.

473

474 **Table 4.** Magnetic parameters from the magnetization isotherm of PANI/Fe₃O₄NPs
 475 composites. The isotherms were measured between -50 and $+50$ kOe at 5 K.

Composite	M_{50} (emu/g) ^{a,b}	M_{rem} (emu/g) ^a	M_{rem} / M_{50}	H_c (kOe)
PANI/NP2	55.2 ± 0.8	–	–	–
PANI/NP10	53.4 ± 0.7	12.8 ± 0.2	0.24 ± 0.02	0.45
PANI/NP27	42 ± 1	6.2 ± 2	0.15 ± 0.04	0.61

476 ^a Mass magnetization referred to the NP mass. ^b The magnetization at 50 kOe
 477 (M_{50}) is far from the saturation value.

478

479

480 *Dynamic electromagnetic absorption and Ferromagnetic resonance*

481 Magnetic materials subjected to an external applied field may show losses attributed to different
 482 phenomena, also frequency dependent. In quasi static conditions, losses are dominated by the
 483 hysteresis loss associated to the reversal of the magnetization direction which occurs whenever
 484 a portion of a domain wall moves between different pinning sites corresponding to two local

485 energy minima and some energy is dissipated to the crystal lattice. Dynamic losses due to the
 486 flow of eddy currents and joule heating within the material under ac excitations are associated
 487 to the magnetic flux variations. At higher frequencies, when flux penetration may be reduced
 488 due to the skin effect, energy dissipation is caused by ferromagnetic resonance, occurring
 489 whenever the frequency of the external ac magnetic field coincides to the Larmor precession
 490 frequency of the magnetization vector. These effects tend to limit the useful frequency range of
 491 magnetic materials in practical devices.

492 Due to their extremely small size, nanosized objects such as NPs do not exhibit large hysteresis
 493 or dynamic losses and can thus be suitable as inductors even above the MHz frequency range.
 494 In fact, NPs with diameters of the order of 10 nm are single domain and magnetization reversals
 495 occur only through rotations, which produce very small dissipation with respect to hysteresis.
 496 Dynamic losses due to large scale eddy currents are also suppressed in NPs, because inter-
 497 particle conduction is hindered by the organic shell and losses arise at frequencies above 1 GHz
 498 only due to the resonant magnetic behavior, and to verify this hypothesis dielectric
 499 characterization was also performed up to the GHz range.

500 The real and imaginary part of the magnetic permeability using the following relations (Fiorillo,
 501 2010):

502

$$503 \quad \mu' = 1 + \frac{Im\{\Delta Z_{in}^*\}}{f\mu_0 h \ln \frac{R_m}{r_m}} \quad (1)$$

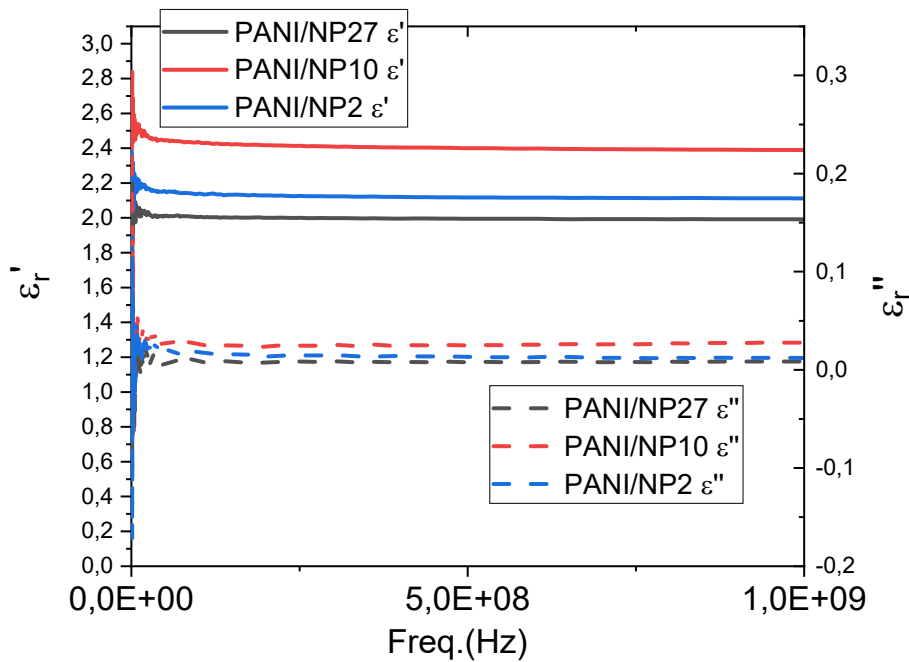
504

$$505 \quad \mu'' = \frac{Re\{\Delta Z_{in}^*\}}{f\mu_0 h \ln \frac{R_m}{r_m}} \quad (2)$$

506

507 where h , R_m and r_m are the thickness, the outside diameter, and the inside diameter of the ring
 508 sample, respectively, $\Delta Z_{in}^* = Z_{in,sample}^* - Z_{in,air}^*$, where $Z_{in,sample}^*$ and $Z_{in,air}^*$ are the circuit
 509 impedances in the the presence or absence of the toroidal sample and f is the frequency.
 510 Capacitance and dielectric properties were determined directly and calibrated through a Teflon
 511 reference, and show that the dielectric properties are constant across the spectrum observed up
 512 to above 1 GHz, without any visible resonant absorption (Figure 7).

513



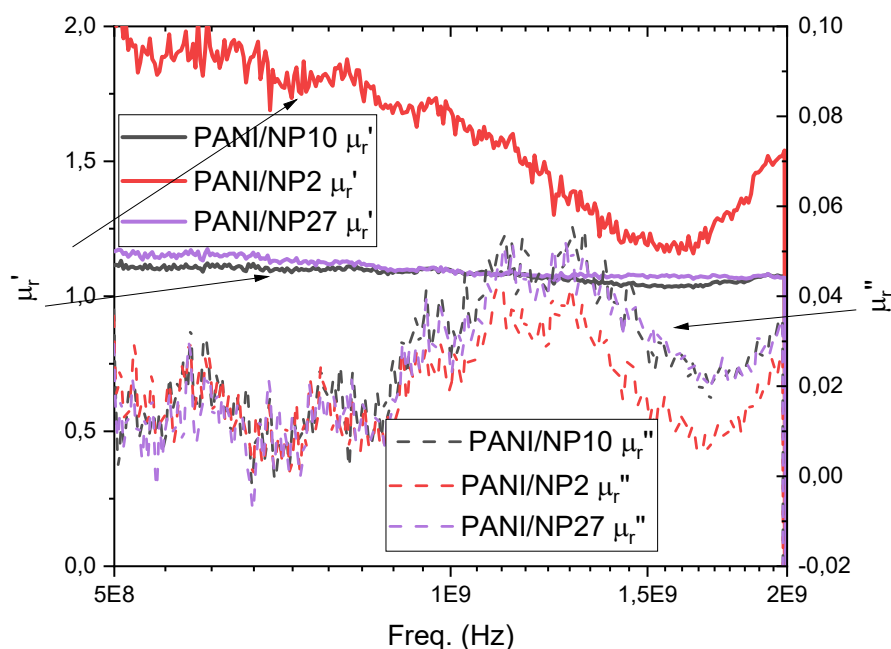
514

515 **Figure 7.** Real (ϵ_r') and imaginary (ϵ_r'') part of the relative permittivity of the PANI/Fe₃O₄NPs
 516 composites. The data exhibits a rather flat behavior up to 1 GHz.

517

518 The ac permeability results (Figure 8) show that PANI/NP2, the composite with 2.3 nm single
 519 domain NPs, with vanishing M_{rem} (Table 4) and higher static initial permeability, has the highest
 520 real part of permeability also in ac. The other samples show relative permeabilities just slightly
 521 above 1. All composites display a wide frequency peak of the imaginary part of the
 522 permeability, which starts below 1 GHz and has a peak at 1.1-1.2 GHz, depending on the
 523 composite, clearly showing that ac losses are only associated to the ferromagnetic resonance.
 524 The large peak width reflects the distribution of particle dimensions and magnetic properties
 525 (also due to exact size, chemical composition, etc.). These results, while compatible with
 526 previous literature (Yun *et al.*, 2014), extend the experimental frequency range explored and
 527 prove that PANI composites with very small Fe oxide particles are instrumental to the
 528 successful use of these materials as energy absorbers in the GHz range.

529



530

531 **Figure 8.** Real (μ_r') and imaginary (μ_r'') part of the relative permeability of the samples. μ_r''
 532 shows an absorption behavior, due to the ferromagnetic resonance, at frequencies slightly above
 533 1 GHz.

534

535

536

Conclusions

537 We have shown that magnetite NPs spanning the size range from 2.3 to 27 nm are able to
 538 catalyze the oxidative polymerization of the aniline dimer and remain within the polymer so to
 539 form PANI/Fe₃O₄ composites. The yields are in all cases high enough to be of practical
 540 importance. Their dependence on the NP surface area shows that i) the NPs are stable against
 541 aggregation in the reaction conditions, ii) the catalytic effect is due to the NPs (and not to Fe³⁺
 542 ions leached into the aqueous phase), and iii) the NPs are a main factor affecting the
 543 polymerization yield. The smallest NPs seem to be not completely stable in the reaction
 544 conditions probably because of their very high surface area that makes them more sensitive to
 545 surface effects such as aggregation and degradation. The embedded NPs retain the shape and
 546 size of the pristine NPs and are well-dispersed in the PANI matrix.

547 The NPs in the composite do not interact by direct exchange, *i.e.*, they retain their magnetic
 548 individuality thanks to the oleic acid coating that prevents direct contact between the NPs. This
 549 enables easy modulation of the composite magnetic properties based on the NP size. Occurrence
 550 of NP direct contact in the composite would have led to unpredictable magnetic properties

551 depending on the details of the polymerization. For the dynamic electromagnetic behavior, the
552 imaginary part of the permeability only shows an absorption, not associated with any dielectric
553 loss, but rather due to the ferromagnetic resonance, at frequencies slightly above 1 GHz. Our
554 synthetic method thus provides a pathway to prepare composites with tailored magnetic
555 properties by customizing the size of the magnetite NPs. It would also be conceivable to prepare
556 composites containing NPs with different size in controlled proportion.

557

558

559 **Funding.** Financial support from Fondazione Cariplo (Milano, Italy) under Grant no. 2012-
560 0872 (Magnetic-nanoparticle-filled conductive polymer composites for EMI reduction) is
561 gratefully acknowledged.

562

563 **Conflict of interest.** The authors declare no conflict of interest.

564

565

Supplementary data

566

567 Electronic Supplementary Material associated with this article can be found in the online
568 version of this paper (DOI: xxxxxxxxxx).

569

570

571 References

- 572 Ahmadkhani L, Mostafavi E, Ghasemali S, Baghban R, Pazoki-Toroudi H, Davaran S,
573 Malakootikhah J, Asadi N, Mammadova L, Saghfi S, Webster TJ, Akbarzadeh A
574 (2019) Development and characterization of a novel conductive polyaniline-g-
575 polystyrene/Fe₃O₄nanocomposite for the treatment of cancer. *Artif Cells Nanomed*
576 *Biotechnol* 47(1):873-881. doi: 10.1080/21691401.2019.1575839
- 577 Bhadra S, Khastgir D, Singha NK, Lee JH (2009) Progress in preparation, processing and
578 applications of polyaniline. *Prog Polym Sci* 34:783–810. doi:
579 10.1016/j.progpolymsci.2009.04.003
- 580 Barbaro D, Di Bari L, Gandin V, Evangelisti C, Vitulli G, Schiavi E, Marzano C, Ferretti AM,
581 Salvadori P (2015) Glucose-coated superparamagnetic iron oxide nanoparticles
582 prepared by metal vapour synthesis are electively internalized in a pancreatic
583 adenocarcinoma cell line expressing GLUT1 transporter *Plos One* 10:e0123159. doi:
584 10.1371/journal.pone.0123159

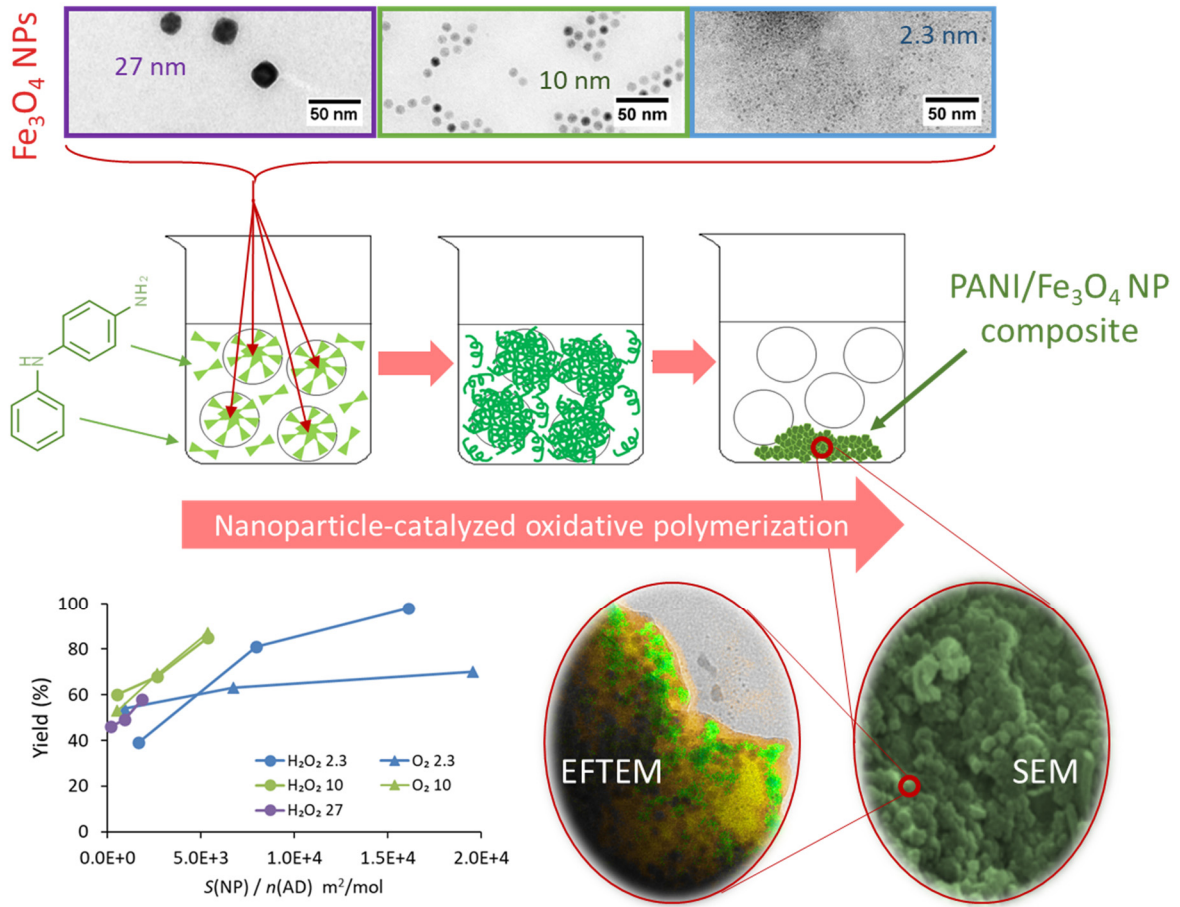
- 585 Bruvera IJ, Mendoza Zélis P, Pilar Calatayud M, Goya GF, Sánchez FH (2015) Determination
586 of the blocking temperature of magnetic nanoparticles: The good, the bad, and the
587 ugly. *J Appl Phys* 118:184304. doi:10.1063/1.4935484
- 588 Campisi S, Palliggiano S, Gervasini A, Evangelisti C (2019) Finely Iron-Dispersed Particles on
589 beta Zeolite from Solvated Iron Atoms: Promising Catalysts for NH₃-SCO. *J Phys*
590 *Chem C* 123:11723-11733. doi: 10.1021/acs.jpcc.9b01474
- 591 Coey JMD (2010) *Magnetism and Magnetic Materials*, Cambridge, Cambridge University
592 Press, p. 266.
- 593 Della Pina C, Rossi M, Ferretti AM, Ponti A, Lo Faro M, Falletta E (2012) One-pot synthesis
594 of polyaniline/Fe₃O₄ nanocomposites with magnetic and conductive behaviour.
595 Catalytic effect of Fe₃O₄ nanoparticles. *Synth Met* 162:2250-2258. doi:
596 10.1016/j.synthmet.2012.10.023; Della Pina C, Falletta E, Ferretti AM, Ponti A,
597 Gentili GG, Verri V, Nesti R (2014) Microwave characterization of magnetically hard
598 and soft ferrite nanoparticles in K-band. *J Appl Phys* 116:154306.
599 doi:10.1063/1.4898138; Della Pina C, Ferretti AM, Ponti A, Falletta E (2015) A green
600 approach to magnetically-hard electrically-conducting polyaniline/CoFe₂O₄
601 nanocomposites. *Compos Sci Technol* 110:138-144. doi:
602 10.1016/j.compscitech.2015.02.007; Della Pina C, De Gregorio MA, Clerici L,
603 Dellavedova P, Falletta E (2018) Polyaniline (PANI): an innovative support for
604 sampling and removal of VOCs in air matrices. *J Hazard Mater* 344:1-8. doi:
605 10.1016/j.jhazmat.2017.10.012
- 606 Dong H, Hu W (2012) *Conducting Polymers: Applications in Electronics and Photovoltaics in*
607 *Book: Encyclopedia of Radicals in Chemistry, Biology and Materials*, Publisher: John
608 Wiley and Sons.
- 609 Evangelisti C, Schiavi E, Aronica LA, Psaro R, Balerna A, Martra G (2015) Solvated Metal
610 Atoms in the Preparation of Supported Gold Catalysts. In: Prati L, Villa A (eds), *Gold*
611 *Catalysis: Preparation, Characterization and Applications*, Jenny Stanford Publishing,
612 Beijing, PRC.
- 613 Falletta E, Ponti A, Sironi A, Ferretti AM, Della Pina C (2015) Nanoferrites as Catalysts and
614 Fillers for Polyaniline/Nanoparticle Composites Preparation. *J Adv Catal Sci Technol*
615 2:8-16. doi: 10.15379/2408-9834.2015.02.02.02
- 616 Ferretti AM, Usseglio S, Mondini S, Drago C, La Mattina R, Chini B, Verderio C, Leonzino
617 M, Cagnoli C, Joshi P, Boraschi D, Italiani P, Li Y, Swartzwelter BJ, Sironi L, Gelosa
618 P, Castiglioni L, Guerrini U, Ponti A (2021) Towards bio-compatible magnetic

- 619 nanoparticles: Immune-related effects, in-vitro internalization, and in-vivo bio-
620 distribution of zwitterionic ferrite nanoparticles with unexpected renal clearance. *J*
621 *Coll Interf Sci* 582:678-700. doi:10.1016/j.jcis.2020.08.026.
- 622 Fiorillo F (2010) Measurements of magnetic materials. *Metrologia* 47:S114–S142.
623 doi:10.1088/0026-1394/47/2/S11
- 624 Hyeon T, Lee SS, Park J, Chung Y, Na H B (2001) Synthesis of highly crystalline and
625 monodisperse maghemite nanocrystallites without a size-selection process. *J Am*
626 *Chem Soc* 123:12798–12801. doi:10.1021/ja016812s
- 627 Ibanez JG, Rincón ME, Gutierrez-Granados S, Chaha M, Jaramillo-Quintero OA, Frontana-
628 Uribe BA (2018) Conducting Polymers in the Fields of Energy, Environmental
629 Remediation, and Chemical–Chiral Sensors. *Chem Rev* 118(9):4731-4816. doi:
630 10.1021/acs.chemrev.7b00482
- 631 Kaur G, Adhikari R, Cass P, Bown M, Gunatillake P (2015) Electrically conductive polymers
632 and composites for biomedical applications. *RSC Adv* 5:37553-37567. doi:
633 10.1039/C5RA01851J
- 634 Li J, Qiao J, Lian K (2020) Hydroxide ion conducting polymer electrolytes and their
635 applications in solid supercapacitors: A review. *Energy Stor. Mater* 24:6-21. doi:
636 10.1016/j.ensm.2019.08.012
- 637 Mišurović J, Mojović M, Marjanović B, Vulić P, Ćirić-Marjanović G (2019) Magnetite
638 nanoparticles-catalysed synthesis of conductive polyaniline. *Synth Met* 257:116174(1-
639 11). doi:10.1016/j.synthmet.2019.116174
- 640 Mondini S, Ferretti AM, Puglisi A, Ponti, A (2012) PEBBLES and PEBBLEJUGGLER:
641 Software for Accurate, Unbiased, and Fast Measurement and Analysis of Nanoparticle
642 Morphology from Transmission Electron Microscopy (TEM) Micrographs. *Nanoscale*
643 4:5356-5372. doi:10.1039/C2NR31276J
- 644 Mondini S, Leonzino M, Drago C, Ferretti AM, Usseglio S, Maggioni D, Tornese P, Chini B,
645 Ponti A (2015) Zwitterion-Coated Iron Oxide Nanoparticles: Surface Chemistry and
646 Intracellular Uptake by Hepatocarcinoma (HepG2) Cells. *Langmuir* 31:7381–7390.
647 doi:10.1021/acs.langmuir.5b01496
- 648 Movassagh-Alanagh F, Bordbar-Khiabani A, Ahangari-Asl A (2017) Three-phase
649 PANI@nano-Fe₃O₄@CFs heterostructure: Fabrication, characterization and
650 investigation of microwave absorption and EMI shielding of PANI@nano-
651 Fe₃O₄@CFs/epoxy hybrid composite. *Compos Sci Technol* 150:65-78. doi:
652 10.1016/j.compscitech.2017.07.010

- 653 Muhammad A, Shah AHA, Bilal S, Rahman G (2019) Basic Blue Dye Adsorption from Water
654 Using Polyaniline/Magnetite (Fe_3O_4) Composites: Kinetic and Thermodynamic
655 Aspects. *Materials*,12:1764(1-26). doi: 10.1039/C7SE00139H10.3390/ma12111764
- 656 Park J, An K, Hwang Y, Park J-G, Noh H-J, Kim J-Y, Park J-H, Hwang N-M, Hyeon T (2004)
657 Ultra-large-scale syntheses of monodisperse nanocrystals. *Nature Mater* 3:891–895.
658 doi:10.1038/nmat1251
- 659 Qiu G, Wang Q, Nie M (2006) Polyaniline/ Fe_3O_4 Magnetic Nanocomposite Prepared by
660 Ultrasonic Irradiation. *J Appl Polym Sci* 102:2107-2111. doi: 10.1002/app.24100
- 661 Tzou K, Gregory RV (1992) Kinetic study of the chemical polymerization of aniline in aqueous
662 solutions. *Synth Met* 47:267-277. doi:10.1016/0379-6779(92)90367-R
- 663 Wang X, Liu Y, Han H, Zhao Y, Mad W, Sun H (2017) Polyaniline coated Fe_3O_4 hollow
664 nanospheres as anode materials for lithium ion batteries. *Sustain. Energy Fuels* 1:915-
665 922. doi: 10.1039/C7SE00139H
- 666 Wang Y, Liu A, Han Y, Li T (2020) Sensors based on conductive polymers and their
667 composites: a review. *Polym Int*, 69:7–17. doi:10.1002/pi.5907
- 668 Wońska M, Szczytko J, Majhofer A, Gosk J, Działkowski K, Twardowski A (2013) Magnetic
669 interactions in an ensemble of cubic nanoparticles: A Monte Carlo study. *Phys Rev B*
670 88:144421. doi:10.1103/PhysRevB.88.144421
- 671 Yang C, Zhang P, Nautiyal A, Li S, Liu N, Yin J, Deng K, Zhang X (2019) Tunable Three-
672 Dimensional Nanostructured Conductive Polymer Hydrogels for Energy-Storage
673 Applications. *ACS Appl Mater Interfaces* 11(4):4258-4267. doi:
674 10.1021/acsami.8b19180
- 675 Yun H, Liu X, Paik T, Palanisamy D, Kim J, Vogel WD, Viescas AJ, Chen J, Papaefthymiou
676 GC, Kikkawa JM, Allen MG, Murray CB (2014) Size- and Composition-Dependent
677 Radio Frequency Magnetic Permeability of Iron Oxide Nanocrystals. *ACS Nano*
678 8:12323-12337. doi:2481/10.1021/nn504711g.
- 679
- 680

681 **Graphical Abstract**

682



683

684

685